Research Paper

GEOSPHERE

GEOSPHERE, v. 18, no. 4

https://doi.org/10.1130/GES02503.1

9 figures; 1 supplemental file

CORRESPONDENCE:
Kaviani@geophysik.uni-frankfurt.de

CITATION: Kaviani, A., Sandvol, E., Ku, W.F., Beck, S.L., Türkelli, N., Özacar, A.A., and Delph, J.R., 2022, Seismic attenuation tomography of the Sn phase beneath the Turkish-Iranian Plateau and the Zagros mountain belt: Geosphere, v. 18, no. 4, p. 1377–1393, https://doi.org/10.1130/GES02503.1.

Science Editor: Andrea Hampel
Associate Editor: Huaiyu Yuan

Received 6 December 2021
Revision received 1 April 2022
Accepted 28 April 2022

Published online 24 June 2022

Seismic attenuation tomography of the Sn phase beneath the Turkish-Iranian Plateau and the Zagros mountain belt

Ayoub Kaviani[1], Eric Sandvol[2], Wenfei Ku[2], Susan L. Beck[3], Niyazi Türkelli[4], A. Arda Özacar[5], and Jonathan R. Delph[6]

[1]Institute of Geosciences, Goethe University Frankfurt, 60323 Frankfurt, Germany
[2]Department of Geological Sciences, University of Missouri, Columbia, Missouri 65211, USA
[3]Department of Geosciences, University of Arizona, Tucson, Arizona 85721, USA
[4]Kandilli Observatory and Earthquake Research Institute, Department of Geophysics, Boğazici University, 34684 Istanbul, Turkey
[5]Department of Geological Engineering, Middle East Technical University, 06800 Ankara, Turkey
[6]Department of Earth, Atmospheric, and Planetary Sciences, Purdue University, West Lafayette, Indiana 47907, USA

ABSTRACT

The Turkish-Iranian Plateau and the Zagros highlands are among the most prominent physiographic features in the Middle East and were formed as a result of continental collision between the Arabian and Eurasian plates. To better understand the nature of the lithospheric mantle and the origin of the observed seismic anomalies in this region, we investigated seismic attenuation of the uppermost mantle by detailed measurements of the quality factor of the Sn seismic phase (Sn *Q*). To that end, we collected a large data set consisting of 30 years (1990–2020) of waveforms recorded by 1266 permanent and temporary seismic stations, applying both the two-station method (TSM) and reverse two-station method (RTM) to measure path-averaged Sn *Q*. Finally, we performed a tomographic inversion on the path-averaged Sn *Q* to map the lateral variations of the upper-mantle attenuation across the northern Middle East. Our Sn attenuation maps show moderately low *Q* (<250) values beneath the Turkish-Iranian Plateau and high *Q* values (>350) beneath the Zagros and northern edge of the Arabian plate. Furthermore, our Sn *Q* model is broadly consistent with seismic velocity models in the region suggesting that most of the seismic anomalies are the result of thermal rather than compositional effects.

INTRODUCTION

The study of seismic attenuation provides a tool for the investigation and characterization of thermal and melting conditions in the upper mantle. Quantifying amplitude reduction of Sn waves provides a unique tool for studying uppermost-mantle attenuation. Sn is a regional seismic phase that can be treated as a guided seismic wave, which principally travels in the uppermost mantle (Molnar and Oliver, 1969; Stephens and Isacks, 1977; Sandvol et al., 2001; Al-Damegh et al., 2004). A variety of important factors can influence the propagation of the Sn phase, including: (1) the vertical gradient in shear wave velocity in the uppermost mantle, (2) the lateral variation in the lithospheric thickness, and (3) the thermal state and the presence of partial melt in the uppermost mantle (Buehler and Shearer, 2013). The attenuation of seismic phases is commonly described by the quality factor *Q* (Knopoff et al., 1964), which is the combined contribution of the intrinsic and scattering attenuation (e.g., Aki and Chouet, 1975; Dainty, 1981). Intrinsic attenuation is attributed mainly to temperature anomaly and the presence of melt and fluids, while scattering attenuation can be caused by structural heterogeneity beneath the region (e.g., Aki, 1980; Fehler et al., 1992; Sato et al., 2012).

The quality factor of the Sn phase (Sn *Q*) can potentially provide an important constraint on the origin of upper-mantle seismic anomalies in the Turkish-Iranian Plateau and surrounding regions (Sandvol et al., 2001; Bao et al., 2011). The Turkish-Iranian Plateau is the dominant tectonic feature in the northern Middle East (Fig. 1) and has been formed by the continental collision between the Arabian and Eurasian plates since the early Cenozoic (23–35 Ma) (Allen et al., 2004; Hatzfeld and Molnar, 2010). Previous studies have suggested that the Turkish-Iranian Plateau is analogous to the Tibetan Plateau, although relatively immature in comparison (Hatzfeld and Molnar, 2010). Similarly, there is a substantial body of work suggesting that the lithospheric mantle is also quite thin beneath the Turkish-Iranian Plateau (e.g., Gök et al., 2003; Al-Lazki et al., 2004; Angus et al., 2006; Priestley and McKenzie, 2013).

The Anatolian Plateau, in the western part of the study area, comprises three main tectonic provinces (Fig. 1): East Anatolian Plateau, Central Anatolian Plateau, and Western Anatolian province. These provinces are mostly underlain by basement of the Anatolide-Tauride, Kirsehir, and Pontide microcontinental fragments that have been amalgamated along various suture zones (e.g., Okay and Tüysüz, 1999). The Bitlis suture zone to the south of the East Anatolian Plateau delineates the boundary between the Eurasian and Arabian plates and represents the final closure of the Neotethys Ocean prior to collision, whereas further to the west, subduction of the African lithosphere beneath the Western Anatolian province and Central Anatolian Plateau along the Aegean (Hellenic) and Cyprean trenches plays an important role in along-strike variations in the morphology and tectonic evolution of the Anatolian Plateau (e.g., Biryol et al., 2011; Portner et al., 2018). Slab rollback along these trenches seems to

Ayoub Kaviani https://orcid.org/0000-0001-5818-1594

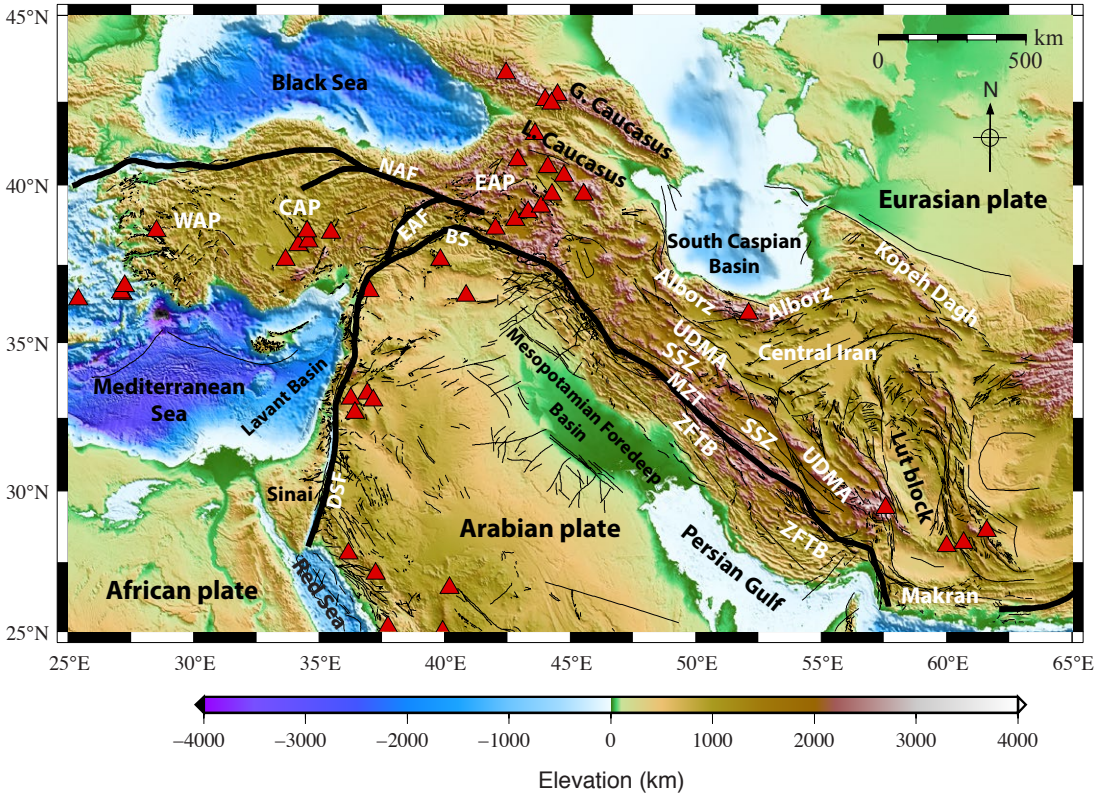

Figure 1. Simplified tectonic map of the Turkish-Iranian Plateau and the eastern Mediterranean. WAP—Western Anatolian province; CAP—Central Anatolian Plateau; EAP—East Anatolian Plateau; BS—Bitlis suture; DSF—Dead Sea fault; NAF—Northern Anatolian fault; EAF—Eastern Anatolian fault; ZFTB—Zagros fold-and-thrust belt; MZT—Main Zagros thrust; SSZ—Sanandaj-Sirjan zone; UDMA—Urumieh-Dokhtar magmatic arc. Red triangles represent Quaternary volcanoes. G. and L. Caucasus stand for Greater and Lesser Caucasus.

contribute to the western escape of the Anatolian block via strike-slip conjugate motions along the Northern Anatolian and Eastern Anatolian fault zones (Burke and Şengör, 1986; Şengör et al., 2005).

The Zagros mountain belt and Iranian Plateau, constituting the eastern part of the Turkish-Iranian Plateau, are composed of the following subparallel tectonic terranes (Allen et al., 2004, 2013), from southwest to northeast (Fig. 1): The Zagros fold-and-thrust belt (ZFTB), the Sanandaj-Sirjan zone, and the Urumieh-Dokhtar magmatic arc, along with other various central Iranian blocks and far-field deformational domains (Alborz, Kopet Dagh). The ZFTB is formed by shortening and subsequent detachment folding of an ~12-km-thick sedimentary package along with reverse faulting in the crystalline basement of the northeastern leading edge of the Arabian plate (Mouthereau, 2011). The Sanandaj-Sirjan zone is bounded by the Main Zagros thrust to the southwest and is considered the major suture between the Arabian and Eurasian plates in Iran (Stöcklin, 1968; Agard et al., 2005; Paul et al., 2006, 2010). The Urumieh-Dokhtar magmatic arc is characterized by Eocene arc volcanism most likely associated with the subduction of the Tethyan oceanic lithosphere beneath Eurasia (Agard et al., 2011). Further east, Central Iran is made up of several aseismic and rigid microblocks (Amini et al., 2012). Part of the convergence between the Arabian and Eurasian plates is accommodated by strike-slip movement between these rigid blocks (Vernant et al., 2004). The far-field areas (Alborz and Kopet Dagh) accommodate the rest of the Arabian-Eurasian convergence (Agard et al., 2011; Vernant et al., 2004). Further to the north, the South Caspian Basin comprises thick sedimentary deposits (~20 km) and is thought to be underlain by oceanic lithosphere (Allen et al., 2003; Gök et al., 2011; Kaviani et al., 2015). Previous studies suggest that the South Caspian Basin is moving westward relative to Central Iran and may be subducting at its northern margin (Jackson et al., 2002b; Allen et al., 2003; Knapp et al., 2004).

Previous studies of regional seismic phases have found slow Pn velocities and high Sn attenuation across the Turkish-Iranian Plateau (Hearn and Ni, 1994; Sandvol et al., 2001; Gök et al., 2003, 2011; Al-Lazki et al., 2004, 2014; Amini et al., 2012; Mutlu and Karabulut, 2011). Low surface- and body-wave velocity anomalies in the uppermost mantle are also observed beneath most of the plateau (Maggi and Priestley, 2005; Hafkensheid et al., 2006; Gök et al., 2007,

2011; Simmons et al., 2011; Delph et al., 2015; Portner et al., 2018; Kaviani et al., 2020). Seismic velocity tomography studies (Maggi and Priestley, 2005; Kaviani et al., 2007; Simmons et al., 2011; Motaghi et al., 2017; Mahmoodabadi et al., 2019) suggest the presence of a thicker and colder lithosphere beneath the Zagros relative to Central Iran. Priestley et al. (2012) argued that the thick "Zagros core" partially accommodates shortening in the mantle. The observed variation in lithospheric thickness can have significant implications for regional mantle flow and deformation (e.g., Kaviani et al., 2021) and the propagation of seismic waves.

So far, only a few studies of high-frequency wave attenuation of the uppermost mantle have been carried out in the Middle East, and most of them have focused on propagation efficiencies rather than on *Q* measurements. Molnar and Oliver (1969) studied the propagation characteristics of Sn waves along regional seismic raypaths using World-Wide Standardized Seismograph Network (WWSSN). They found efficient Sn propagation in stable regions such as continental shields and deep oceanic basins, whereas paths crossing Iran and Turkey were typically characterized by Sn blockage. In a more detailed study, Kadinsky-Cade et al. (1981) studied the propagation characteristics of regional seismic phases in the Middle East using WWSSN seismograms and observed efficient Sn beneath a major part of the Turkish-Iranian Plateau; however, the Sn phase was strongly attenuated beneath the eastern and northern parts of the Anatolian Plateau and the northern part of Iranian Plateau. Rodgers et al. (1997) improved upon Kadinsky-Cade et al. (1981)'s work by including data from the Iranian Long Period Array and Global Seismic Network stations. They also observed efficient Sn propagation across oceanic lithosphere while Sn appeared blocked or inefficient within the Turkish-Iranian Plateau. They suggested that this is in part due to partial melting in the upper mantle beneath the Anatolian and northern Iranian Plateaus. Sandvol et al. (2001) and Al-Damegh et al. (2004) studied the propagation efficiency of Sn in the Middle East and also observed Sn blockage across most of the Turkish-Iranian Plateau along with efficient Sn across the South Caspian Basin and Arabian plate. More recently, Gök et al. (2003, 2011) added data from the Eastern Turkey Seismic Experiment stations to the study of Sandvol et al. (2001) and thus improved the Sn sampling throughout the Turkish-Iranian Plateau. These studies also reported efficient Sn propagation along the ZFTB and found Sn was largely blocked throughout the Anatolian Plateau.

In this study, we analyzed a large waveform database for the northern Middle East and quantified Sn *Q* to characterize the uppermost mantle shear wave attenuation across the region. We collected and processed more than two decades of regional seismograms from more than 1260 seismic stations of permanent networks and temporary deployments across the broad region of the northern Middle East. The combined data set from the Turkish-Iranian Plateau and northern Arabian plate provided the unique opportunity for obtaining an integrated image of the uppermost mantle attenuation structure beneath the region. The Sn attenuation model presented in our study is largely consistent with previous studies but at a much higher sampling density and with more reliable absolute *Q* estimates than previous studies.

DATA AND METHODS

The waveform data used in this study were collected from 1266 seismic stations operated across the Turkish-Iranian Plateau (Fig. 2). We analyzed Sn seismograms from 7160 regional crustal (<40 km) seismic events, all with body-wave magnitudes (M_b) >4.5. In total, 149,000 seismograms were visually examined for data quality, and only those seismograms with a clear Pn arrival were selected for the Sn spectrum calculation. The Sn window was then automatically picked by a search algorithm that selects the best window as defined by having the maximum signal-to-noise ratio within predefined limits based on a range of Sn velocity values between 4.3 km/s and 4.7 km/s.

In the first step, the propagation efficiency of all Sn seismograms was determined in order to identify Sn blockage for particular raypaths. To measure the propagation efficiency of Sn phases, we applied a band-pass filter (0.3–2.0 Hz) to all seismograms and characterized Sn phases into three categories: efficient, inefficient, and blocked). If the seismogram contained no Sn energy, it was characterized as "blocked Sn". If there was a clear change in amplitude and frequency within the Sn velocity window, we designated it as "efficient Sn". If there was an ambiguous signal that could potentially be an Sn signal, it was classified as "inefficient Sn". In Figure 3, we show the event-to-station paths color coded according to their efficiency. The blue and green paths denote efficient and inefficient Sn propagation, respectively; the red paths mean Sn blockage. Because these event-to-station paths cross different tectonic domains, it is difficult to untangle where the main attenuation or blockage occurs along each path.

We used the results of the efficiency categorization to identify and exclude two-station paths where there is no apparent Sn phase at the station nearest to an event. Pasyanos et al. (2009) pointed out that by discarding blocked seismic data resulting from high attenuation, the resulting model can be biased toward higher *Q* values compared to the real values. Conversely, by including these raypaths, large model errors could be generated due to including amplitudes of noise and coda. We posit that when there is no clear Sn phase observed at the near station, the amplitude ratio between the two stations may not be representative of the Sn *Q* along the two-station path. We, therefore, decided to exclude two-station paths with a blocked Sn at the near station.

We then measured the effective quality factor (*Q*) on the remaining data along the individual paths between two stations (and two events). We followed two approaches to calculate the effective path-based *Q* values: (1) two-station method (TSM) and (2) reverse two-station two-event method (RTM); we briefly describe these methods below. The interested reader is referred to Kaviani et al. (2015) and Tiwari et al. (2022) for detailed descriptions of these methods.

The *Q* measurement is based on the initial assumption that the amplitude of the given phase (here Sn) is calculated according to the following convolutional relation in the spectral (frequency) domain:

$$A(f) = S(f)E(f)\Delta^{-m}e^{\left(\frac{-\pi f\Delta}{vQ(f)}\right)}, \quad (1)$$

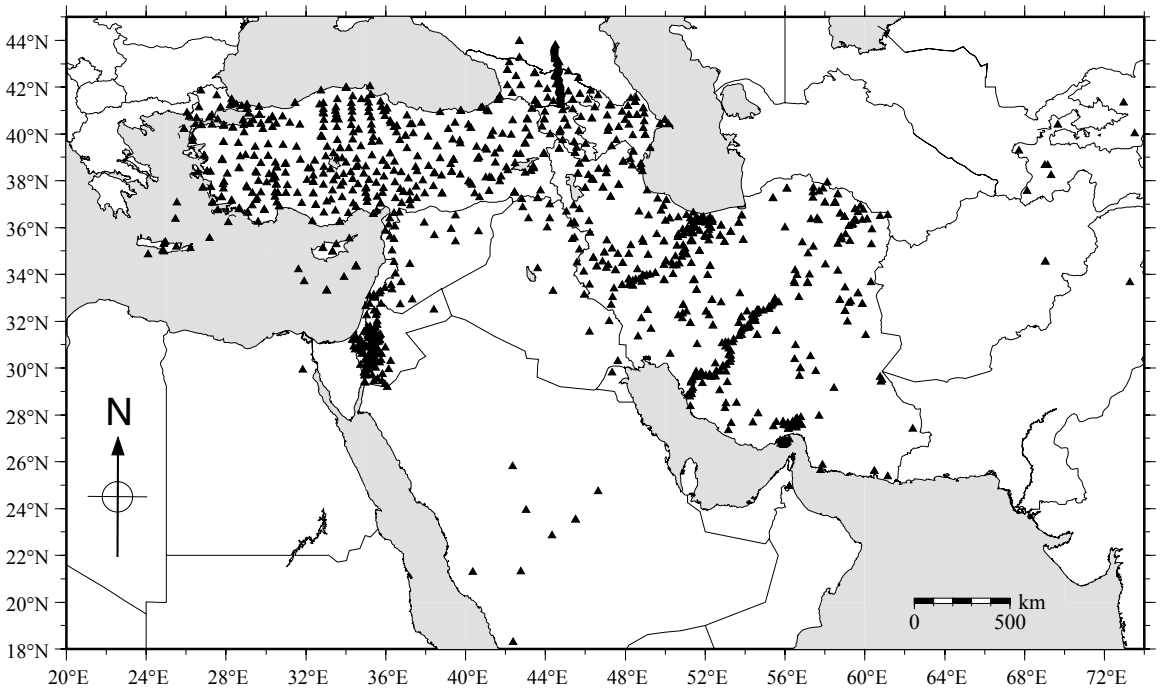

Figure 2. Map showing the seismic stations (black triangles) used in this study.

where f is the central frequency, $S(f)$ is the frequency-dependent site term (including instrument response), $E(f)$ is the frequency-dependent source spectrum, Δ is the epicentral distance, m is a geometrical spreading factor, v is the wave propagation group velocity (4.5 km/s), and $Q(f)$ is the frequency-dependent quality factor (representing the effective seismic attenuation). We assume a geometrical spreading factor, m, of 1.0 as is suggested by numerical simulations (e.g., Yang et al., 2007) for high-frequency Sn waves.

In the TSM approach, the frequency-dependent Sn Q can be calculated by dividing the spectra at two stations generated from an event occurring along the great circle path connecting the stations:

$$\frac{A_i(f)}{A_j(f)} = \frac{S_i(f)}{S_j(f)}\left(\frac{\Delta_i}{\Delta_j}\right)^{-m} e^{\left(\frac{-\pi f \Delta_{ij}}{vQ(f)}\right)}, \quad (2)$$

where A_i/A_j is the spectral amplitude ratio between the near station i and the far station j, and $\Delta_{ij} = \Delta_j - \Delta_i$ is the epicentral distance difference (which is close to the interstation distance). The source spectrum term $E(f)$ is removed during the spectral division because it is the same between the two stations. The site term ratio $S_i(f)/S_j(f)$ can be assumed to be 1 after the removal of the instrument response, assuming that the site conditions at the two stations are comparable to each other. Then, the frequency-dependent Sn Q can be calculated using the TSM approach as:

$$\frac{1}{Q(f)} = \frac{-v}{\pi f \Delta_{ij}} \ln\left[\frac{A_i(f)}{A_j(f)}\left(\frac{\Delta_i}{\Delta_j}\right)^{m}\right]. \quad (3)$$

The frequency dependence of Sn Q is usually assumed to have the form of a power-law equation (e.g., Aki and Chouet, 1975; Shito et al., 2004):

$$Q(f) = Q_0 f^{\eta}, \quad (4)$$

where η is the frequency-dependent factor and Q_0 is Q at 1 Hz. By replacing the left side of Equation 3 with the inverse of the right side of Equation 4 and taking the logarithm, we obtain:

$$(1-\eta)\ln f - \ln Q_0 = \ln\left\{\frac{-v}{\pi \Delta_{ij}} \ln\left[\frac{A_i(f)}{A_j(f)}\left(\frac{\Delta_i}{\Delta_j}\right)^{m}\right]\right\}. \quad (5)$$

By applying a linear regression to the measurements (right side of Equation 5), the quality factor at 1 Hz (Q_0) and the frequency-dependent factor η can be obtained.

Figure 3 is interactive. Please open the PDF with Adobe Reader or Acrobat. Raypaths can be toggled on and off using the Acrobat (PDF) Layers panel in the Acrobat navigation pane (vertical bar on left side of window). Click the "Layers" icon to display available layers; turn layers on or off by clicking the box to the left of the layer name. If the interactivity does not work in the version of the paper you are reading, please visit https://doi.org/10.1130/GEOS.S.20137805.

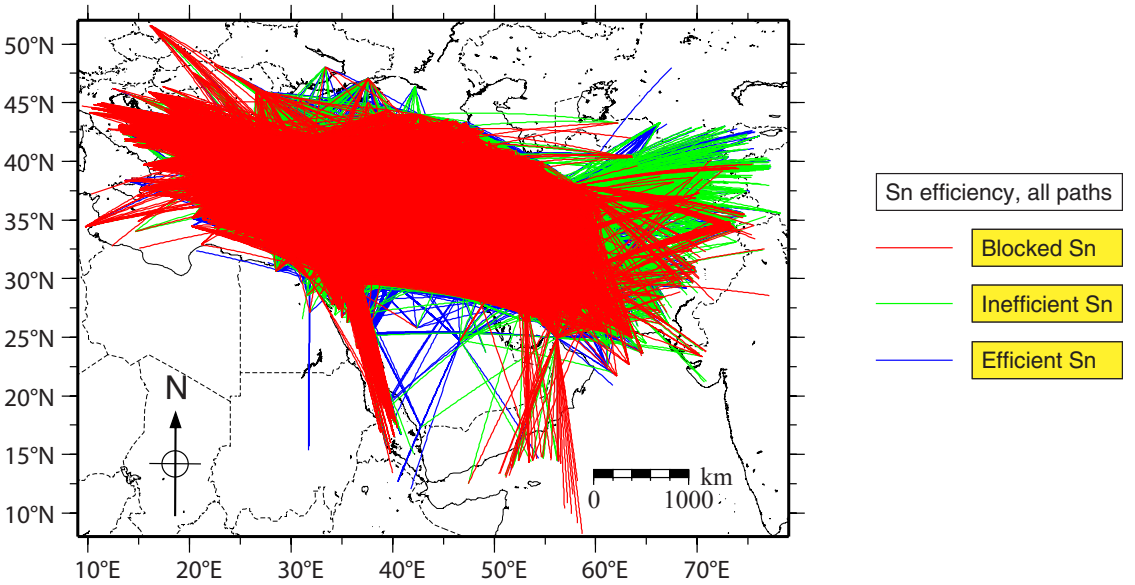

Figure 3. (interactive) Map of raypaths with Sn propagation efficiencies. Raypaths are color coded according to their respective efficiency (red, blocked Sn; green, inefficient Sn; blue, efficient Sn). If the interactivity does not work in the version of the paper you are reading, please visit https://doi.org/10.1130/GEOS.S.20137805.

Incorrect instrument responses and/or different site conditions at the two stations can potentially lead to a site term ratio ($S_i(f)/S_j(f)$ in Equation 2) much different from 1.0. This difference in site term between the two stations can bias the Q measurements in the TSM approach. This is typically caused when the instrument response at one or both stations is incorrect. In an attempt to eliminate the potential effect of differing site terms, the reverse two-station method (RTM) was proposed by Chun et al. (1987). In the RTM approach, we need to have Sn phase spectra from two events located on opposite sides of the station pair along the great circle path. By multiplying the Sn spectral ratios of the two stations from the two events, the frequency-dependent Sn Q can be calculated as:

$$\frac{1}{Q(f)} = \frac{v}{\pi f\left(\Delta_{aj} - \Delta_{ai} - \Delta_{bj} + \Delta_{bi}\right)} \ln\left[\frac{A_{ai}(f)}{A_{aj}(f)}\frac{A_{bj}(f)}{A_{bi}(f)}\left(\frac{\Delta_{ai}\Delta_{bj}}{\Delta_{aj}\Delta_{bi}}\right)^{m}\right], \quad (6)$$

where A_{ai}, A_{aj}, A_{bi}, and A_{bj} denote spectral amplitudes of Sn recorded at stations i and j for events a and b, and Δ_{ai}, Δ_{aj}, Δ_{bi}, and Δ_{bj} are corresponding epicentral distances. It is straightforward to obtain an expression (as in Equation 5 for the TSM geometry) so that a linear regression of the observables (combination of spectral ratios and epicentral distances) gives estimates for the Q value and the frequency-dependent factor (η). The effect of relative site terms on the Q calculation is eliminated in the RTM measurements. These terms represent the difference in local site conditions between stations and/or remaining uncorrected instrument responses, and we are able to estimate their relative value using RTM.

After calculation of the Sn Q at 0.5 Hz, 1 Hz, and 2 Hz using both the TSM and RTM approaches, we then discarded TSM Q estimates at stations that showed anomalously large site terms based on the RTM calculation to avoid biasing the Q locally in the tomography models. In the next step, we applied a screening analysis to compare Sn Q measurements for spatially proximate paths for both the remaining TSM and RTM data sets. If a single Q measurement along a path was larger than twice the standard deviation away from the mean Q value for other proximate paths, the measurement was discarded. Using this analysis, the outliers for raypaths in a localized area were identified and discarded from the data set. After this screening process, 25% of the individual measurements were identified as outliers and discarded. Because many of these individual measurements are repeated along a given raypath, the total number of two-station paths for the final tomography is reduced by only <3%.

In both the TSM and RTM methods, multiple measurements are obtained for many of the station pairs. In this case, we used the mean value of the measurements at that station pair. The final averaged path-based inter-station Sn Q values for a central frequency of 1 Hz are presented in Figure 4. The TSM and RTM paths, color coded according to their Q values, are shown in

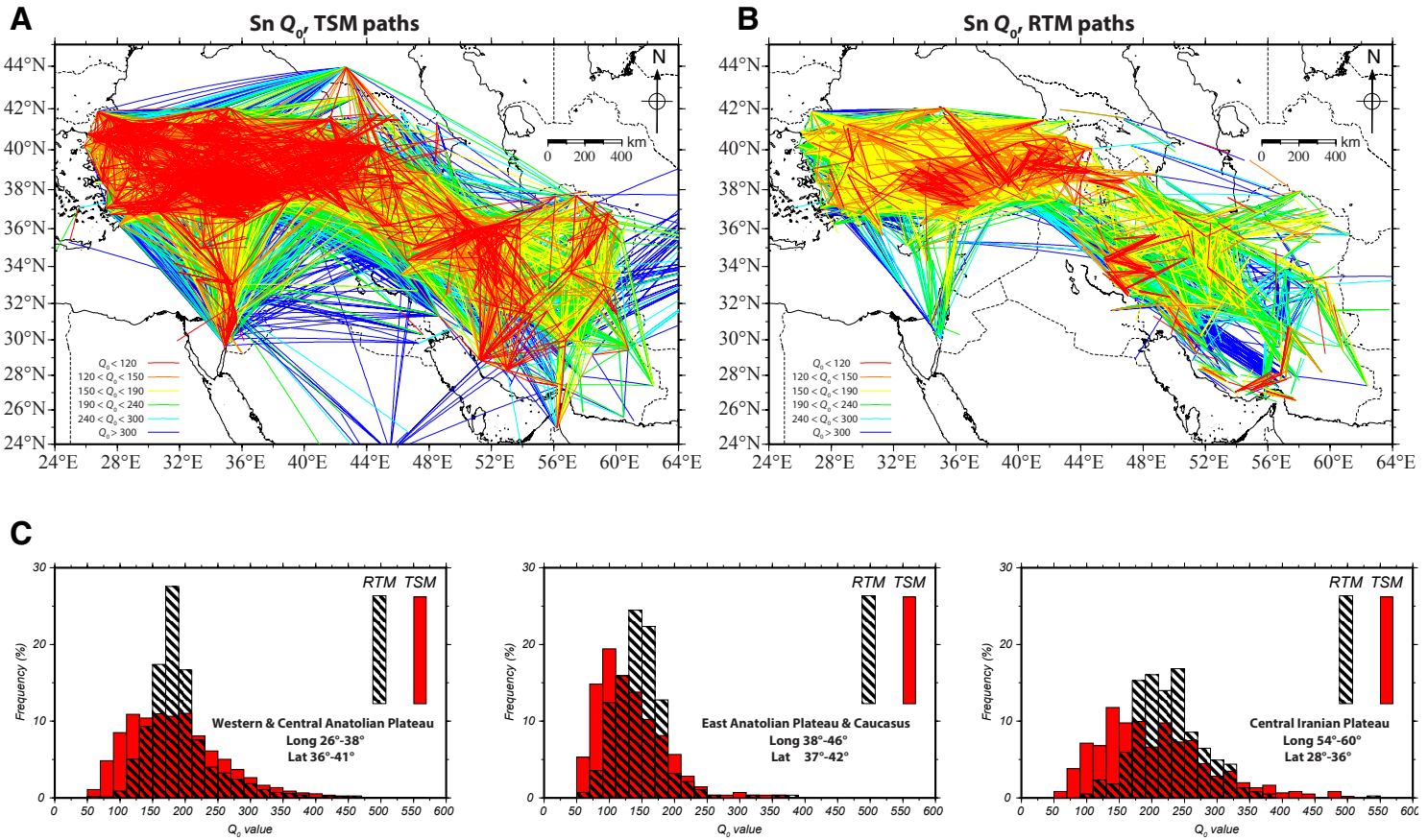

Figure 4. (A and B) Two-station method (TSM) (A) and reverse two-station method (RTM) (B) paths color coded according to their Sn quality factor (Q_0) values. Ranges of values are shown in the maps. (C) Histograms representing the distribution of the TSM (red) and RTM (hachured) measurements along raypaths crossing three selected regions: Western Anatolian province and Central Anatolian Plateau (left), East Anatolian Plateau and Caucasus (middle), and central Iranian Plateau (right).

Figures 4A and 4B, respectively. The main goal of presenting the raypaths is to compare the data coverage in the two methods. The actual lateral variation of the attenuation is mapped via tomographic inversion of the individual ray-averaged *Q* values, as discussed in the next sections. The TSM ray coverage is very dense across the entire study area except for the Arabian plate. Both data sets densely sample the Turkish-Iranian Plateau but only sparsely sample the margins of the study area. The raypaths provide the first indication that most of the Anatolian Plateau is mainly characterized by low Sn *Q* values. The Iranian Plateau is also mainly covered by low *Q* values, though some regions are partially covered by paths with relatively higher Sn *Q* values. The northern Arabian plate has high Sn *Q* for the TSM model but ray sampling in this region for the RTM model is too low to validate this observation. In order to quantitatively compare the distribution of the path-averaged *Q* estimates, we also show in Figure 4C the distribution of the TSM and RTM measurements along raypaths crossing three selected regions. We observe two main features in all regions: (1) the RTM measurements present a narrower distribution than the TSM measurements, partially due to uncorrected site effects on the TSM *Q* estimates, and (2) the RTM measurements tend to have a higher mean value relative to the TSM method. In western and central Anatolia, the RTM values give an average Q_0 value well centered between 150 and 200, while the TSM paths give an average value widely defined between 100 and 200. In the East Anatolian Plateau and the Caucasus, the RTM paths give a mean value around

150 whereas the TSM paths give a lower mean value around 100. In the central Iranian Plateau, the RTM measurements are clearly shifted to higher values with a mean value between 200 and 250, while the TSM paths present a wide distribution with a mean value <150.

Finally, we performed a least-squares inversion on the interstation frequency-dependent Sn *Q* estimates to obtain two-dimensional maps of attenuation in the study area (Paige and Saunders, 1982; Xie and Mitchell, 1990; Chun et al., 1987; Kaviani et al., 2015). The damping parameter for this inversion was set to 3 after examining several values and verifying the trade-off between the data variance and model resolution.

RESULTS

The tomographic maps of Sn *Q* at 1 Hz obtained using the TSM and RTM geometries are shown in Figures 5A and 5B, respectively. Figure 5C presents the difference between the TSM and RTM maps (Figs. 5A and 5B) in areas with common coverage. In order to verify the stability and errors of the Sn *Q* models, we performed a bootstrap resampling test (Hearn and Ni, 1994; Sandvol et al., 2001; Kaviani et al., 2015). The results of the bootstrap uncertainty maps are shown in Figure 6. The uncertainty maps show that in the regions with high ray coverage (Fig. 4; Fig. S1[1]), the uncertainty is generally <15% of the absolute *Q* values (across the entire region of the Anatolian Plateau and most of Central Iran), whereas it can be >20% for regions with sparse ray coverage such as the northern Arabian plate, southern Zagros, southeastern Iran, the Caspian Sea, and the Greater Caucasus.

In addition to the bootstrap analysis, we performed synthetic tests to examine the resolution of our Sn *Q* model. In Figure 7, we present two sets of synthetic tests: (1) a checkerboard model and (2) a model with an arbitrary distribution of *Q* anomalies simulating the anomalies derived from the results presented in Figure 5. The checkerboard test (Figs. 7A–7C) indicates that Sn *Q* anomalies with a size of 2° × 2° can be well resolved in the regions with good ray coverage (across the majority of the Turkish-Iranian Plateau). The synthetic *Q* anomalies are distorted in the regions with limited azimuthal coverage, as would be expected. The synthetic test with an arbitrary distribution of *Q* anomalies (Figs. 7D–7F) suggests that the local anomalies across the Anatolian and Iranian Plateaus are generally well constrained.

The Sn *Q* models at 1.0 Hz obtained from the TSM and RTM measurements (Fig. 5) exhibit similar large-scale features, though they are different in terms of small-scale heterogeneities and the absolute value of the *Q* anomalies. We consider the RTM Sn *Q* map (Fig. 5B) more reliable because this method should be less affected by erroneous site terms. However, the TSM results can provide insight into the attenuation structure of regions that are not well sampled via the RTM analysis. For regions sampled by both data sets, the largest differences are seen around the ZFTB and the eastern Mediterranean (Fig. 5C). These differences are largely due to significant variations in ray coverage between the data sets (Fig. 4; Fig. S1, footnote 1) where bootstrap resampling prior to inversion also indicates large uncertainties in the absolute values of Sn *Q* (Fig. 6), and synthetic tests (Fig. 7) also denote low resolution and smearing of the *Q* models in these regions.

The model of Sn *Q* at 1 Hz (Q_0) (Fig. 5) shows significant lateral variations in the upper-mantle attenuation beneath the Turkish-Iranian Plateau. Across most of the Anatolian Plateau, we observe low Sn *Q* values (<250). Areas of very low *Q* values (<150) in the East Anatolian Plateau and Lesser Caucasus correlate well with the location of Neogene volcanism (Keskin, 2003; Şengör et al., 2003; Schleiffarth et al., 2018). These low–Sn *Q* regions extend eastward into the northwestern Iranian Plateau. Previous studies indicated that Pn velocities in this region are also below the global average (Hearn and Ni, 1994; Amini et al., 2012). A region of low Sn *Q* values (<150) is also found in the Levant Basin (northeastern corner of the Mediterranean) that is bounded to the east by the Dead Sea fault zone. This low–Sn *Q* region in the eastern Mediterranean looks like an extension of the low *Q* region of central Anatolia, which may broadly correspond with volcanism in the Central Anatolian volcanic province (Innocenti et al., 1975; Schleiffarth et al., 2018).

Central Iran is mainly characterized by Sn *Q* values between 150 and 300, close to the values observed in central and western Anatolia. The RTM paths in Central Iran tend to give higher values relative to the TSM raypaths, as also shown in Figure 4C. The Lut block in eastern Central Iran (Fig. 1 for location) is characterized by higher Sn *Q* relative to other parts of Central Iran.

In the ZFTB, we generally observe high Sn *Q* values (>400) with some significant lateral heterogeneity. These variations are manifested in discrepancies between the TSM and RTM maps (Fig. 5C). One main reason for this discrepancy across the ZFTB may be the relatively long inter-station distances, where the differences in site condition at the two stations can be large and significantly affect the TSM *Q* measurements. High *Q* estimates (>400) are also observed across the northern Arabian plate, although we only have TSM results in this region and the uncertainty is relatively high (Fig. 6A). Below the South Caspian Basin, both the TSM and RTM approaches show high Sn *Q* (>400) along with high uncertainties (Fig. 6) due to the poor path density.

By measuring Sn *Q* at different frequencies, we are able to verify the frequency dependence of attenuation. Sn *Q* maps obtained from the TSM and RTM methods at three different central frequencies (0.5 Hz, 1.0 Hz, and 2.0 Hz) are shown in Figure 8. We see that *Q* generally increases with increasing frequency, as expected. In western and central Anatolia, Sn *Q* increases from a mean value of ~150 at 0.5 Hz to a mean value of ~300 at 2.0 Hz, whereas it changes with frequency in a narrow range between ~100 and ~150 in eastern Anatolia. In Central Iran, we observe Sn *Q* values ranging from ~150 at 0.5 Hz to ~350 at 2.0 Hz, comparable to what we observe in central Anatolia. We observe relatively higher values in the ZFTB with significant along-strike variations at all frequencies.

[1]Supplemental Material. Figure S1: Maps showing ray coverage per model block. Please visit https://doi.org/10.1130/GEOS.S.19686957 to access the supplemental material, and contact editing@geosociety.org with any questions.

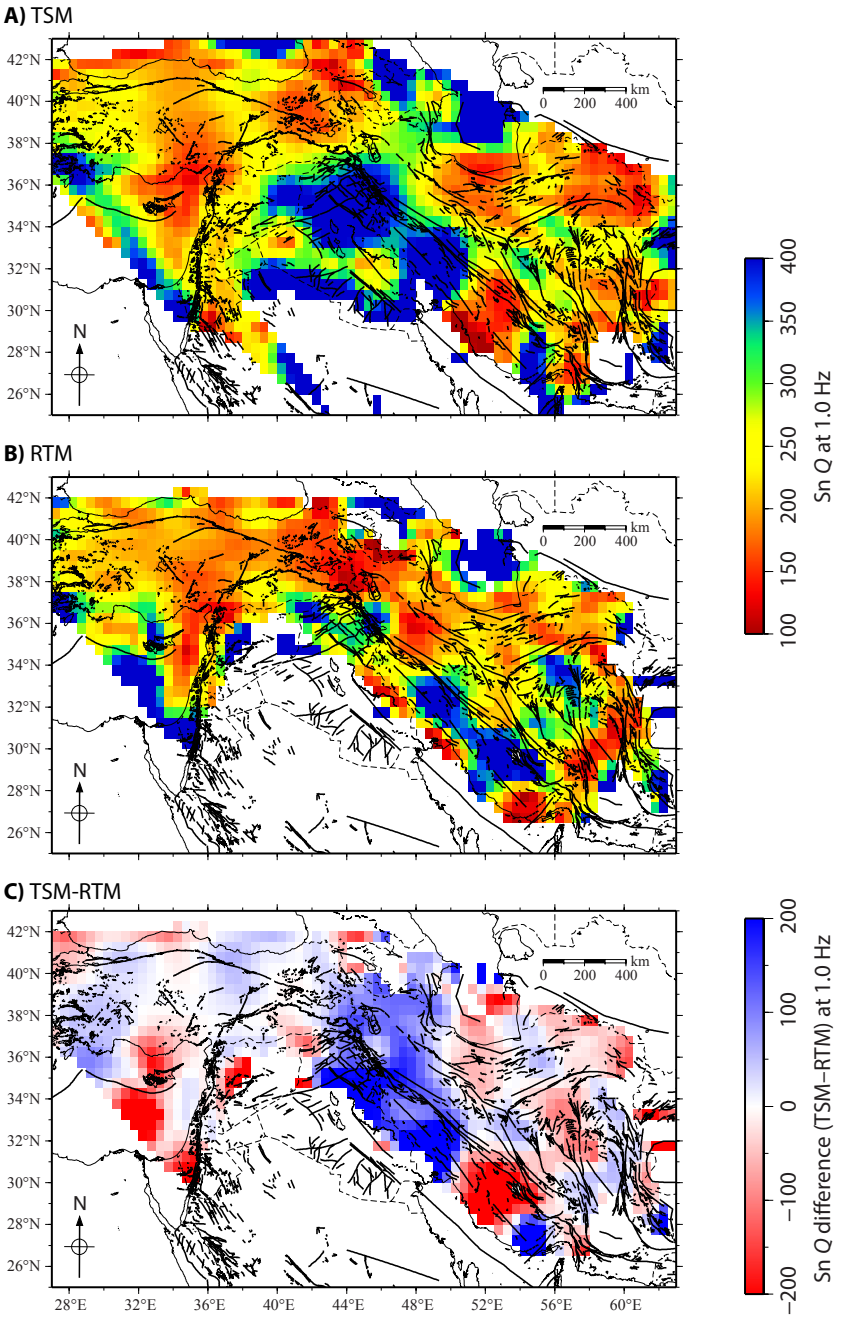

Figure 5. (A) Two-station method (TSM) Sn *Q* tomographic map (at 1.0 Hz); high *Q* is low attenuation and vice versa. (B) Reverse two-station method (RTM) Sn *Q* tomographic map. (C) Difference between the TSM and RTM maps. Thick black lines indicate major faults in the northern Middle East; thin black lines indicate coastlines; thin dashed lines indicate country boundaries.

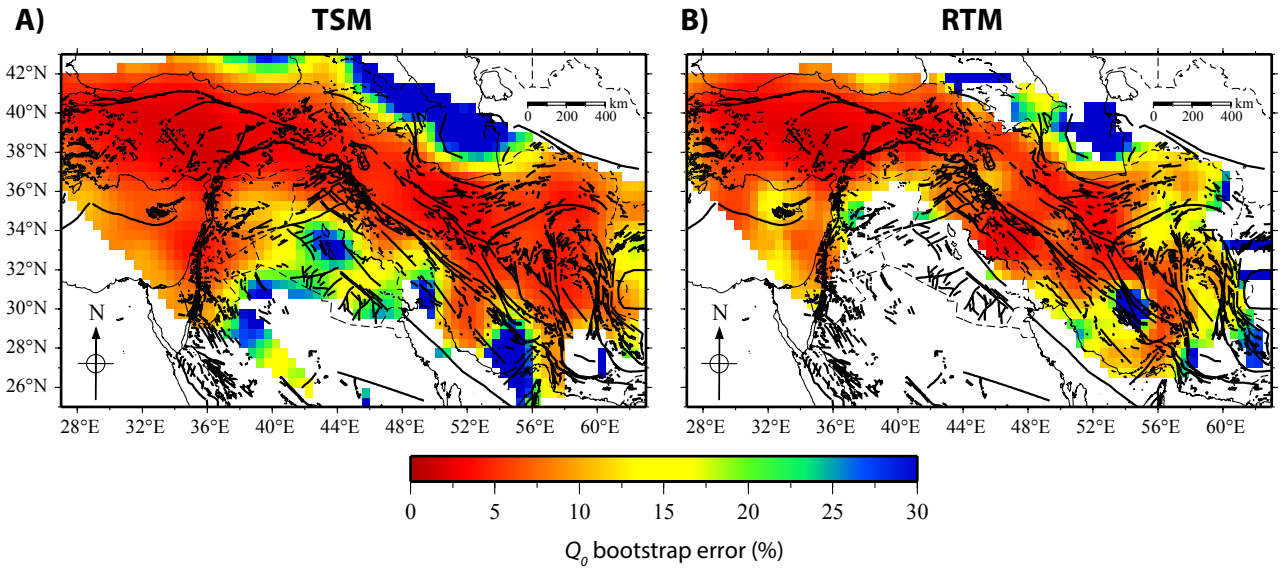

Figure 6. Maps showing the standard deviations computed by bootstrap analysis for the two-station method (TSM) (A) and reverse two-station method (RTM) (B) Sn *Q* (at 1.0 Hz) tomographic models. Thick black lines indicate major faults; thin black lines indicate coastlines; thin dashed lines indicate country boundaries.

A detailed inspection of the Sn *Q* variation with frequency in different parts of the study area requires mapping of the frequency-dependent factor (η). While we can map the lateral variation of η by a tomographic inversion of the path-averaged η values (using an assumption of linearity), the relationship between η and path length is in reality nonlinear. Therefore, we follow another approach based on Equation 4 to calculate η directly from the frequency-dependent Sn *Q* models shown in Figure 8. In Figure 9, we compare the η obtained from the Sn *Q* maps (Figs. 9B and 9D) and those obtained by direct tomographic inversion (Figs. 9A and 9C). Though the two sets of maps share common features in the central regions of the models, the nonlinear nature of the frequency dependence manifests itself mainly as discrepancies between the two models at the borders. We also observe differences between the η maps obtained from the TSM and RTM geometries (Fig. 9B and 9D) in some regions, indicating that uncorrected site terms in the TSM method have effects not only on the *Q* but also on the η estimates. Overall, the η values vary between –0.2 and 1.0 across the entire model, with the lowest values found across the East Anatolian Plateau.

In western and central Anatolia as well as across the central Iranian Plateau, we observe a gentle increase of Sn *Q* with frequency that is clear on both the Sn *Q* and η maps (Figs. 8 and 9). The northwestern region of the ZFTB and northern edge of the Arabian plate are generally characterized by high Sn *Q* anomalies at all frequencies whose limits are delineated by the Main Zagros thrust–Bitlis suture in the east and north and the Dead Sea fault zone in the west. The RTM η map (Fig. 9D) also shows a clear distinction between the southern and northern ZFTB. We also observe a region of relatively high frequency dependence of Sn *Q* in the northern edge of the Arabian plate, seen in the TSM η map (Fig. 9B). Better ray coverage may be required to verify the robustness of the lateral variations in mantle attenuation structure along the ZFTB.

DISCUSSION

It is generally assumed that the seismic properties of the mantle are likely controlled by the temperature of the medium through which the waves propagate. However, other physical properties, such as compositional variations and the presence of melt and fluids, may also play a significant role in determining seismic anomalies in the continental mantle (e.g., Artemieva et al., 2004). Positive temperature anomalies ("hotter" material) should lead to higher attenuation and lower velocity; however, this anticorrelation between attenuation and velocity may not be the case if the seismic properties are controlled by composition rather than temperature (Artemieva et al., 2004; Nakajima and Hasegawa, 2003). Furthermore, lateral variation in mantle structure can give rise to scattering of seismic waves that manifests itself in the reduction of the coherent arrival of Sn energy.

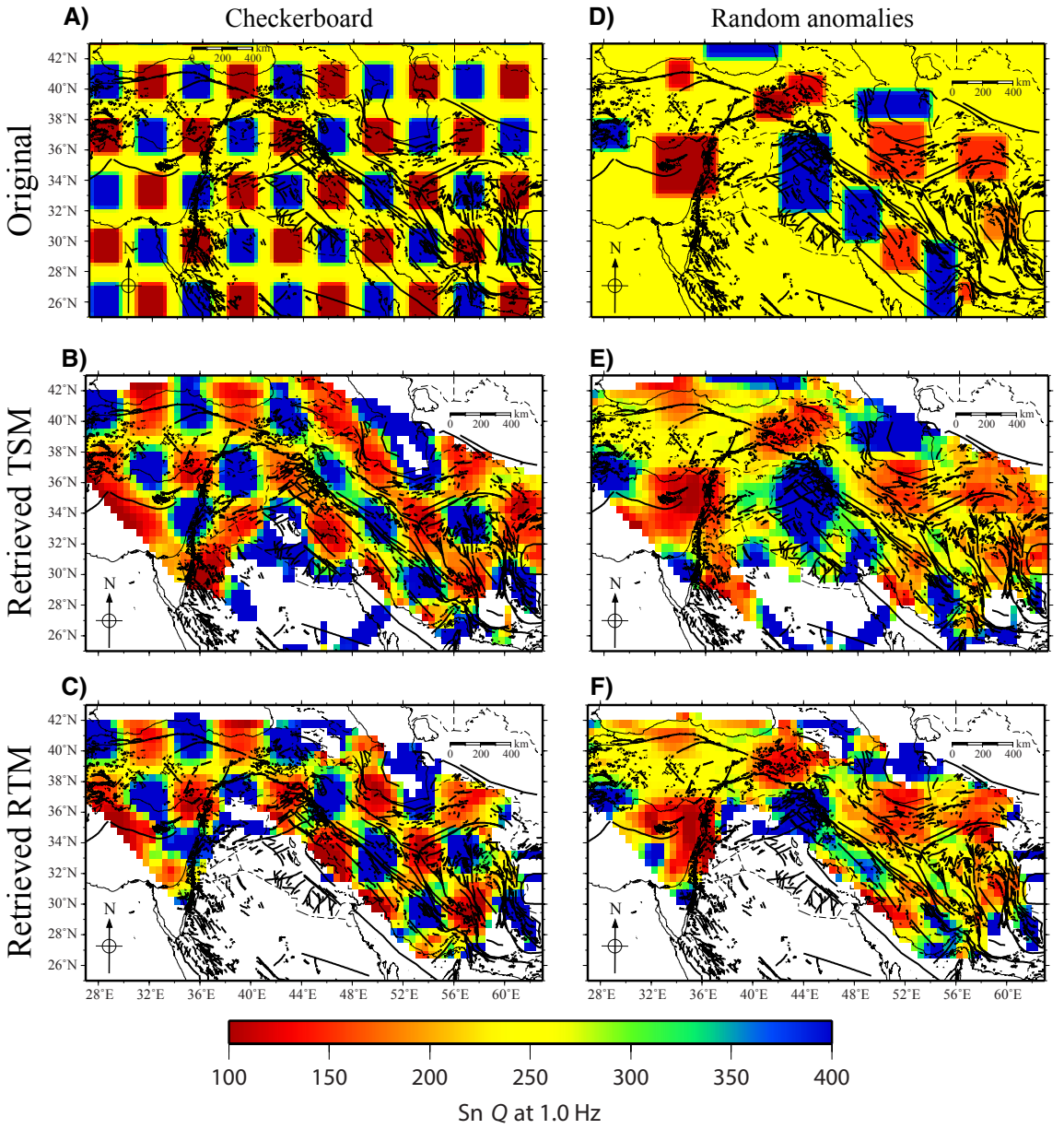

Figure 7. Synthetic models of Sn quality factor (*Q*) for the two-station method (TSM) and reverse two-station method (RTM). (A–C) Checkerboard model with the block size of 2° × 2° (A) and corresponding retrieved models using the TSM and RTM raypaths (B and C, respectively). (D–F) Randomly distributed anomalies with arbitrary sizes (D) and corresponding retrieved models using the TSM and RTM raypaths (E and F, respectively). Thick black lines indicate major faults; thin black lines indicate coastlines; thin dashed lines indicate country boundaries.

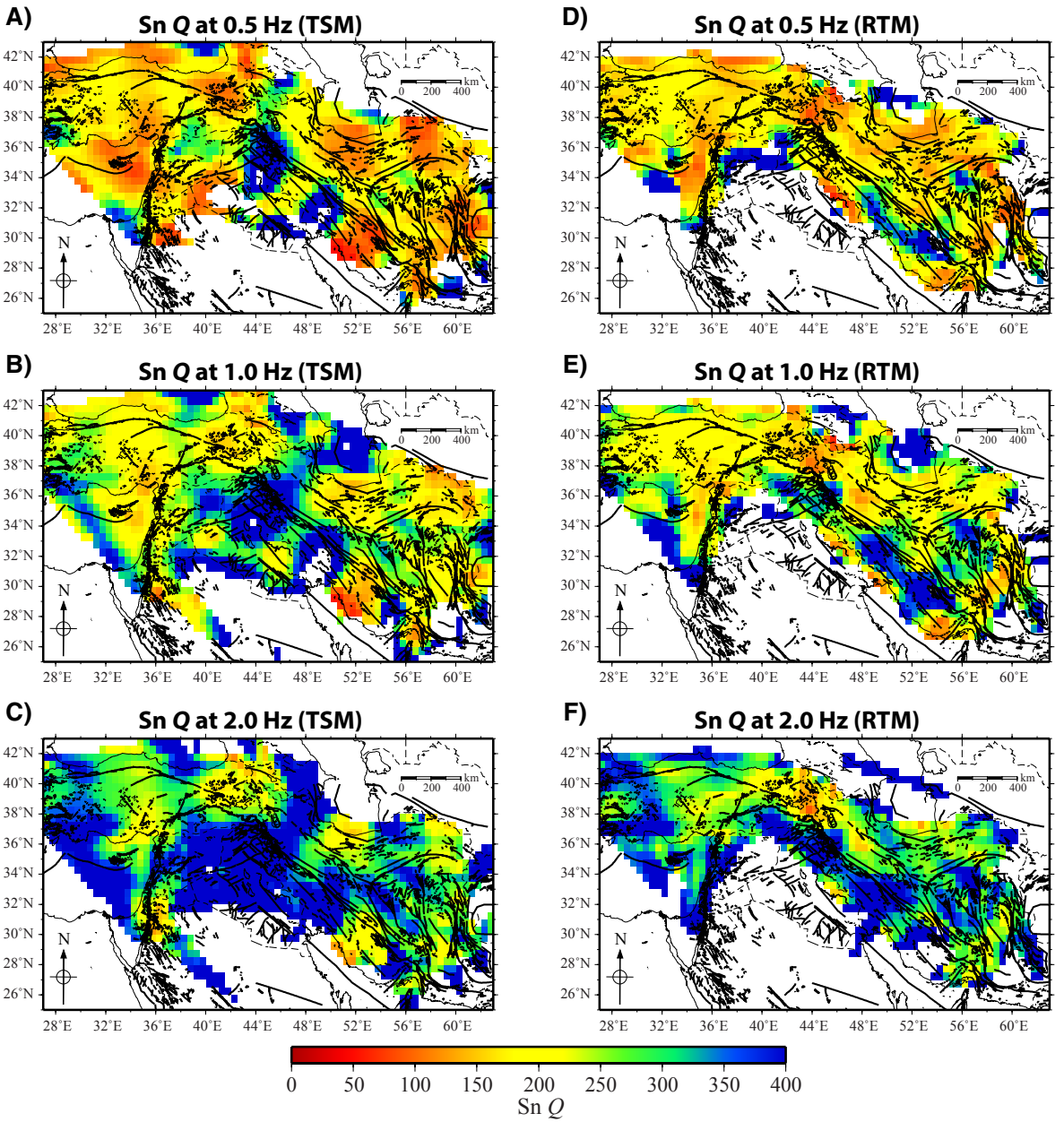

Figure 8. (A–C) Sn quality factor (*Q*) tomographic maps from the two-station method (TSM) at 0.5 Hz (A), 1 Hz (B), and 2 Hz (C). (D–F) Same for the reverse two-station method (RTM). Thick black lines indicate major faults; thin black lines indicate coastlines; thin dashed lines indicate country boundaries.

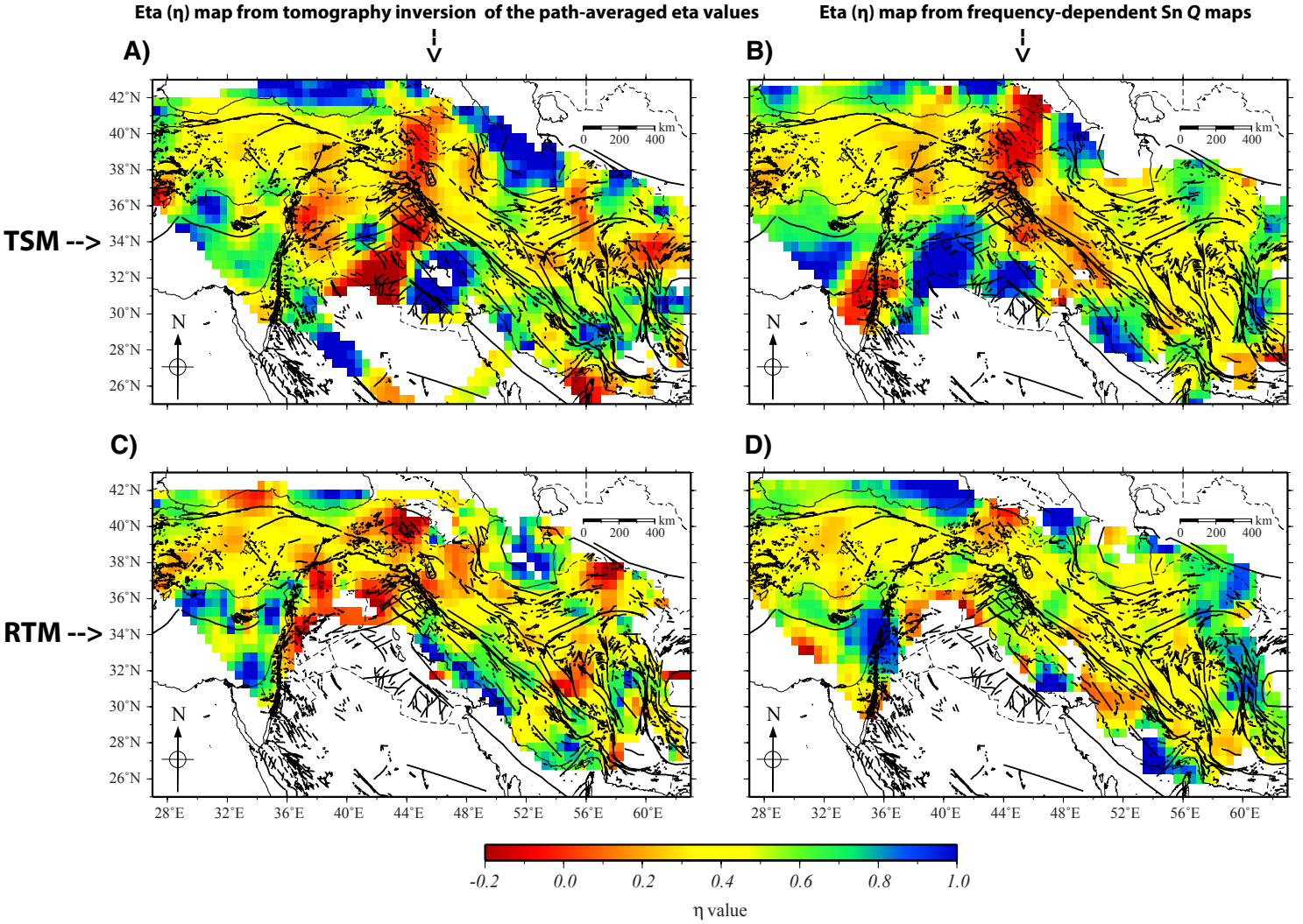

Figure 9. Frequency-dependent factor (η) maps as obtained from the direct tomographic inversion of the path-averaged η values (left column, A and C) or from the Sn quality factor (*Q*) maps (right column, B and D) for the two-station method (TSM) (upper row, A and B) and reverse two-station method (RTM) (lower row, C and D) methods. Thick black lines indicate major faults; thin black lines indicate coastlines; thin dashed lines indicate country boundaries.

We compare our Sn attenuation model with previous seismic velocity models to address the origin of the uppermost-mantle seismic anomalies beneath the study area. The Sn attenuation model presented in our study is spatially consistent with the large-scale features of previously published Sn Q models (Sandvol et al., 2001; Gök et al., 2003, 2011). However, our model has far better ray coverage than previous studies because we incorporate a significantly longer duration of seismic measurements along with denser station distribution. Sn Q is relatively low (<250) across most of the Turkish-Iranian Plateau and increases to >500 beneath the Zagros mountain belt and regions with oceanic basins such as the Black Sea and South Caspian Basin. The real values of Sn Q in high-attenuation regions can be lower than our estimated values given that we discarded paths with blocked Sn, which are indicative of strong attenuation. Furthermore, our data set and model parametrization give smoothed models with resolution that can be lower than the size of small-scale real Q anomalies in the upper mantle.

Seismic attenuation is a frequency-dependent phenomenon (e.g., Aki and Chouet, 1975; Dainty, 1981). Investigation of frequency-dependent Sn Q allows inference, to some extent, of the nature of the seismic attenuation in the upper mantle. Intrinsic attenuation is generally characterized by weak frequency dependence while scattering attenuation corresponds to strong frequency dependence (Barron and Priestley, 2009; Bao et al., 2011; Kaviani et al., 2015). Across most of our model, η is low to normal (0–0.5), suggesting that intrinsic attenuation is the dominant mechanism for the seismic attenuation in the uppermost mantle beneath the Turkish-Iranian Plateau. Laboratory experiments on dry upper-mantle compositions suggest that η can vary between 0.2 and 0.5 depending on temperature and average grain size, while the presence of melt tends to reduce the frequency dependence (η ~0; e.g., Jackson et al., 2002a; Jackson et al., 2004; Faul et al., 2004). On the other hand, seismological observations show that η in the upper mantle can vary between 0.2 and 1.0 depending on the penetration depth and geometry of the raypath as well as on the three-dimensional velocity structure of the medium (e.g., Martynov et al., 1999; Cheng and Kennett, 2002; Shito et al., 2004). Our η maps suggest that intrinsic attenuation is the dominant mechanism in the upper mantle beneath the Turkish-Iranian Plateau. In regions with abrupt lateral variations in the lithospheric thickness, such as beneath the northwestern Zagros and at the edges of the oceanic basins, we see some evidence indicating that scattering is the dominant mechanism of attenuation.

Below the East Anatolian Plateau, the strong attenuation of Sn and weak frequency dependence is consistent with observations of low Pn velocities (e.g., Hearn and Ni, 1994; Amini et al., 2012; Mutlu and Karabulut, 2011) and slow body-wave velocities (Gök et al., 2007; Biryol et al., 2011; Salaün et al., 2012; Delph et al., 2015, 2017; Portner et al., 2018; Kaviani et al., 2020). These slow velocities have been interpreted as the result of the presence of a hot uppermost mantle beneath the Anatolian Plateau. This interpretation is consistent with the observed low Sn Q at all frequencies (Fig. 8) and weak frequency dependence (Fig. 9). These seismic characteristics are observed in a region of widespread Miocene to recent magmatism (e.g., Schleiffarth et al., 2018) characterized largely by very shallow melt pressure-temperature equilibria from young volcanism (Reid et al., 2017, 2019), providing further evidence that the uppermost mantle beneath the East Anatolian Plateau is hot and likely contains partial melt. This interpretation is consistent with the notion of shallow asthenosphere beneath a thinned and/or absent lithospheric mantle lid, possibly due to the detachment and sinking of a segment of the Tethyan slab and subsequent upwelling of the asthenosphere (e.g., Şengör et al., 2003; Bartol and Govers, 2014; Delph et al., 2017). By comparing our Sn Q model with crustal Q models from Lg and Pg waves (Zor et al., 2007; Kaviani et al., 2015; Bao et al., 2011), we find some consistent features suggesting a causal link between crustal and uppermost-mantle attenuation. In the Lesser Caucasus and Eastern Anatolian Plateau, the observation of very low Q values in all three models (Sn, Lg, and Pg), in agreement with low seismic-wave velocities in the crust and upper mantle, strongly suggests the presence of partial melting in both the crust and uppermost mantle. This can be caused by the proximity of crustal material with the asthenosphere, given that the lithospheric mantle below the East Anatolian Plateau appears to be very thin or even absent (Şengör et al., 2003; Angus et al., 2006).

Beneath the Central Anatolian Plateau and Western Anatolian province, we observe higher Sn Q (~250) relative to the East Anatolian Plateau, also consistent with the presence of higher S-wave velocities (Delph et al., 2015, 2017; Kaviani et al., 2020). The frequency dependence is also moderate (~0.4) in the Central Anatolian Plateau and Western Anatolian province, suggesting that intrinsic attenuation is the main cause of dissipation of Sn wave energy. These lines of evidence imply the presence of a colder and/or more stable lithospheric mantle beneath the region relative to the East Anatolian Plateau. Further to the southwest, we observe a small region of relatively high Sn Q along the Hellenic subduction zone, possibly resulting from the presence of the subducting slab, given that the mantle wedge of the upper plate is likely too thin to have a significant effect on Sn propagation. On the other hand, serpentinization in the mantle wedge can have significant effect on seismic velocity and attenuation; however, degree of serpentinization varies in different subduction zones (Xia et al., 2015). Evidence for high seismicity in the mantle wedge beneath the Hellenic subduction zone (e.g., Halpaap et al., 2018) can be indicative for a relatively low degree of serpentinization and, therefore, for a low degree of seismic attenuation.

The eastern Mediterranean and surrounding coastal areas show significant lateral heterogeneity (Figs. 5, 8). Based on synthetic tests and a qualitative inspection of our ray coverage (Figs. 4, 7), only the northeastern portion of the Mediterranean (including the island of Cyprus and the Levant Basin) appear to be well resolved. The low–Sn Q region of Central Anatolia seems to extend southward into the northeastern Mediterranean. The Dead Sea fault zone delineates a clear boundary between the low-Q region of the Levant Basin and the higher-Q region of the northern Arabian plate. S-wave velocities near the Levant Basin area are also characterized by a relatively high-velocity uppermost mantle (e.g., Kaviani et al., 2020). The observation of low Sn Q and high seismic velocities along with a strong frequency dependence in the same area

(Fig. 9D) suggests that the low Sn Q is likely a result of scattering rather than intrinsic attenuation. The nature of the lithosphere beneath the Levant Basin is complex, with a crust that may consist of both oceanic and continental fragments (e.g., Segev et al., 2018). This complex lithosphere appears to transition to purely oceanic lithosphere near the western edge of Cyprus (Granot, 2016). Higher-resolution images of the velocity and attenuation structures of the crust and upper mantle are needed to learn more about the architecture of the lithospheric mantle beneath this region.

In the ZFTB, we generally observe efficient Sn propagation (high Sn Q). Along-strike variations are also present beneath the ZFTB in both Sn Q and η maps (Figs. 8 and 9); however, our current ray coverage does not have sufficient azimuthal sampling to indicate whether Sn propagation direction contributes to the observed variations. The northern edge of the Arabian plate and the northwestern ZFTB show a large region of high Sn Q at all frequencies that is bordered by the Main Zagros thrust–Bitlis suture zone to the east and north and the Dead Sea fault zone to the west (Fig. 8). If the relatively strong frequency dependence of Sn Q in the northern edge of the Arabian plate seen in the TSM η map (Fig. 9B) is robust, it is likely due to the scattering of Sn energy at the edge of the thick Arabian lithosphere (Maggi and Priestley, 2005; Kaviani et al., 2007; McKenzie and Priestley, 2016).

Further to the northeast within the Sanandaj-Sirjan zone and Urumieh-Dokhtar magmatic arc, the Q values decrease and the propagation of Sn waves shifts from inefficient propagation to blockage. Our Sn Q model is consistent with seismic velocity models (Maggi and Priestley, 2005; Kaviani et al., 2007; Simmons et al., 2011; Motaghi et al., 2017; Mahmoodabadi et al., 2019) that show a transition from a higher-velocity upper mantle beneath the ZFTB to a lower-velocity upper mantle beneath Central Iran. In the central Iranian Plateau, Sn waves either propagate inefficiently or are partially blocked at all frequencies, resulting in relatively low Q values (Fig. 8) and low frequency-dependent factor (Fig. 9). Pn velocity is near the global average beneath Central Iran (Hearn and Ni, 1994; Amini et al., 2012), and uppermost-mantle S-wave velocity is also higher than that of eastern Anatolia (Priestley and McKenzie, 2013; Kaviani et al., 2020). These observations could indicate the presence of a relatively high-temperature upper mantle hosting localized, colder pieces of lithospheric mantle detached from the subducted Neotethys slab during the late Miocene (e.g., Agard et al., 2011; Mahmoodabadi et al., 2019). We also surmise that the uppermost mantle beneath Central Iran may be in a subsolidus thermal condition, which prevents extensive partial melting.

While resolution tests indicate that the reliability of our results decreases as we approach the South Caspian Basin, some general observations can be made from the tomographic maps. We observe low Sn Q along the Alborz mountain belt that continues to the southern edge of the South Caspian Basin (Fig. 8). This may imply that the upper-mantle structure beneath the Alborz extends below the South Caspian Basin. The shear-wave velocity model from Kaviani et al. (2020) also suggests that although the South Caspian Basin and Alborz appear to have distinct structures at shallower depths (<60 km), the deeper mantle structure below the South Caspian Basin is more similar to that of the Alborz and Central Iran rather than of the Eurasian plate. The Sn Q is relatively high in the northern part of the South Caspian Basin, though the resolution of our models is not sufficient to resolve small-scale changes. The region of relatively high η values (>0.7) in the western edge of the basin (Fig. 9) is likely due to the scattering of Sn waves at the transition from oceanic to continental lithosphere (Isacks and Stephens, 1975; Stephens and Isacks, 1977; Dainty, 1981). As previous studies have also suggested (e.g., Maggi and Priestley, 2005; Gök et al., 2011; Kaviani et al., 2015, 2020), better data coverage around and across the South Caspian Basin is required to robustly address the nature of the lithosphere (oceanic or continental) beneath this region.

CONCLUSIONS

We made use of a large Sn waveform data set to investigate the upper-mantle attenuation structure beneath the broad region of the northern Middle East including the Iranian and Anatolian Plateaus. Frequency-dependent path-averaged Sn Q values were computed between station (and event) pairs using two methods: TSM (two-station method) and RTM (reversed two-station method). The path-averaged Q values were then tomographically inverted to map lateral variations in Sn Q beneath the region of study. Our high-resolution frequency-dependent Sn Q maps place new constraints on the upper-mantle structure beneath the region. The following main concluding remarks can be drawn from our study:

- Our frequency-dependent Sn Q models suggest that intrinsic attenuation is the main mechanism of seismic attenuation across the Turkish-Iranian Plateau, though scattering attenuation also plays an important role in the regions such as beneath the Zagros fold-and-thrust belt and at the edges of the oceanic basins.
- The East Anatolian Plateau is characterized by a highly attenuative uppermost mantle consistent with the observation of low seismic velocities. The correlated low-velocity and high-attenuation anomalies and the presence of Quaternary volcanism suggest the occurrence of widespread partial melting beneath the East Anatolian Plateau.
- The uppermost mantle beneath the central and western Anatolian Plateau and the central Iranian Plateau is also characterized by high attenuation, though it is less attenuative than the upper mantle beneath the East Anatolian Plateau. The observation of a less-attenuative and a higher-velocity upper mantle relative to the East Anatolian Plateau suggests colder conditions and less-extensive partial melting.
- Relatively high Sn Q and strong frequency dependence are observed beneath the Zagros fold-and-thrust belt and northern Arabian plate, which can be indicative of a stable and thick lithosphere with a distinct boundary and abrupt lateral variation in thickness relative to the neighboring regions including Central Iran and the East Anatolian Plateau.
- The regions underlain by oceanic lithosphere including the Black Sea and South Caspian Basin exhibit a low-attenuation upper mantle, implying a stable and cold mantle lithosphere.

- The Levant Basin and Cyprus microcontinent in the eastern Mediterranean are characterized by relatively low Sn *Q* values and strong frequency dependence, suggesting significant structural heterogeneity in the upper mantle that causes strong scattering of Sn waves.

ACKNOWLEDGMENTS

This research was supported by U.S. National Science Foundation grant EAR-1109336 and AFRL (Air Force Research Laboratory) contract FA9453-11-C-0235. Figures presented in the paper were created using GMT software (http://www.soest.hawaii.edu/gmt/) and Matlab. Regional event seismograms were collected from multiple seismic networks in the region. Data from the Kandilli Observatory Digital Broadband Seismic Network and Israeli Broadband Seismological Network were downloaded from the European Integrated Data Archive (EIDA; https://www.orfeus-eu.org/data/eida/). The seismograms from the permanent stations in Iran were directly downloaded from the Iranian Seismological Center (http://irsc.ut.ac.ir). The facilities of IRIS Data Services and specifically the IRIS Data Management Center (https://ds.iris.edu/ds/nodes/dmc/) were used to get data from temporary stations and the few global permanent stations used in this study. We are also very grateful to the associate editor and two anonymous reviewers for their careful and constructive comments, which helped us improve the manuscript and clarify our discussion.

REFERENCES CITED

Agard, P., Omrani, J., Jolivet, L., and Mouthereau, F., 2005, Convergence history across Zagros (Iran): Constraints from collisional and earlier deformation: International Journal of Earth Sciences, v. 94, p. 401–419, https://doi.org/10.1007/s00531-005-0481-4.

Agard, P., Omrani, J., Jolivet, L., Whitechurch, H., Vrielynck, B., Spakman, W., Monié, P., Meyer, B., and Wortel, R., 2011, Zagros orogeny: A subduction-dominated process: Geological Magazine, v. 148, p. 692–725, https://doi.org/10.1017/S001675681100046X.

Aki, K., 1980, Attenuation of shear-waves in the lithosphere for frequencies from 0.05 to 25 Hz: Physics of the Earth and Planetary Interiors, v. 21, p. 50–60, https://doi.org/10.1016/0031-9201(80)90019-9.

Aki, K., and Chouet, B., 1975, Origin of coda waves: Source, attenuation, and scattering effects: Journal of Geophysical Research, v. 80, p. 3322–3342, https://doi.org/10.1029/JB080i023p03322.

Al-Damegh, K., Sandvol, E., Al-Lazki, A., and Barazangi, M., 2004, Regional seismic wave propagation (Lg and Sn) and Pn attenuation in the Arabian Plate and surrounding regions: Geophysical Journal International, v. 157, p. 775–795, https://doi.org/10.1111/j.1365-246X.2004.02246.x.

Al-Lazki, A.I., Sandvol, E., Seber, D., Barazangi, M., Türkelli, N., and Mohamad, R., 2004, Pn tomographic imaging of mantle lid velocity and anisotropy at the junction of the Arabian, Eurasian and African plates: Geophysical Journal International, v. 158, p. 1024–1040, https://doi.org/10.1111/j.1365-246X.2004.02355.x.

Al-Lazki, A.I., Al-Damegh, K.S., El-Hadidy, S.Y., Ghods, A., and Tatar, M., 2014, Pn-velocity structure beneath Arabia–Eurasia Zagros collision and Makran subduction zones, *in* Rollinson, H.R., Searle, M.P., Abbasi, I.A., Al-Lazki, A.I., and Al Kindi, M.H., eds., Tectonic Evolution of the Oman Mountains: Geological Society of London Special Publication 392, p. 45–60, https://doi.org/10.1144/SP392.3.

Allen, M., Jackson, J., and Walker, R., 2004, Late Cenozoic reorganization of the Arabia-Eurasia collision and the comparison of short-term and long-term deformation rates: Tectonics, v. 23, TC2008, https://doi.org/10.1029/2003TC001530.

Allen, M.B., Vincent, S.J., Alsop, G.I., Ismail-zadeh, A., and Flecker, R., 2003, Late Cenozoic deformation in the South Caspian region: Effects of a rigid basement block within a collision zone: Tectonophysics, v. 366, p. 223–239, https://doi.org/10.1016/S0040-1951(03)00098-2.

Allen, M.B., Saville, C., Blanc, E.J.-P., Talebian, M., and Nissen, E., 2013, Orogenic plateau growth: Expansion of the Turkish-Iranian Plateau across the Zagros fold-and-thrust belt: Tectonics, v. 32, p. 171–190, https://doi.org/10.1002/tect.20025.

Amini, S., Shomali, Z.H., Koyi, H., and Roberts, R.G., 2012, Tomographic upper-mantle velocity structure beneath the Iranian Plateau: Tectonophysics, v. 554–557, p. 42–49, https://doi.org/10.1016/j.tecto.2012.06.009.

Angus, D.A., Wilson, D.C., Sandvol, E., and Ni, J.F., 2006, Lithospheric structure of the Arabian and Eurasian collision zone in eastern Turkey from *S*-wave receiver functions: Geophysical Journal International, v. 166, p. 1335–1346, https://doi.org/10.1111/j.1365-246X.2006.03070.x.

Artemieva, I.M., Billien, M., Lévêque, J.-J., and Mooney, W.D., 2004, Shear wave velocity, seismic attenuation, and thermal structure of the continental upper mantle: Geophysical Journal International, v. 157, p. 607–628, https://doi.org/10.1111/j.1365-246X.2004.02195.x.

Bao, X.Y., Sandvol, E., Zor, E., Sakin, S., Mohamad, R., Gök, R., Mellors, R., Godoladze, T., Yetirmishli, G., and Türkelli, N., 2011, Pg attenuation tomography within the northern Middle East: Bulletin of the Seismological Society of America, v. 101, p. 1496–1506, https://doi.org/10.1785/0120100316.

Barron, J., and Priestley, K., 2009, Observations of frequency-dependent S_n propagation in Northern Tibet: Geophysical Journal International, v. 179, p. 475–488, https://doi.org/10.1111/j.1365-246X.2009.04318.x.

Bartol, J., and Govers, R., 2014, A single cause for uplift of the Central and Eastern Anatolian plateau?: Tectonophysics, v. 637, p. 116–136, https://doi.org/10.1016/j.tecto.2014.10.002.

Biryol, C.B., Beck, S.L., Zandt, G., and Özacar, A.A., 2011, Segmented African lithosphere beneath the Anatolian region inferred from teleseismic P-wave tomography: Geophysical Journal International, v. 184, p. 1037–1057, https://doi.org/10.1111/j.1365-246X.2010.04910.x.

Buehler, J.S., and Shearer, P.M., 2013, *Sn* propagation in the Western United States from common midpoint stacks of USArray data: Geophysical Research Letters, v. 40, p. 6106–6111, https://doi.org/10.1002/2013GL057680.

Burke, K., and Şengör, A.M.C., 1986, Tectonic escape in the evolution of the continental crust, *in* Barazangi, M., and Brown, L., eds., Reflection Seismology: The Continental Crust: American Geophysical Union Geodynamics Series 14, p. 41–53.

Cheng, H.X., and Kennett, B.L.N., 2002, Frequency dependence of seismic wave attenuation in the upper mantle beneath the Australian region: Geophysical Journal International, v. 150, p. 45–57, https://doi.org/10.1046/j.1365-246X.2002.01677.x.

Chun, K.Y., West, G.F., Kokoski, R.J., and Samson, C., 1987, A novel technique for measuring Lg attenuation—Results from eastern Canada between 1 to 10 Hz: Bulletin of the Seismological Society of America, v. 77, p. 398–419, https://doi.org/10.1785/BSSA0770020398.

Dainty, A.M., 1981, A scattering model to explain seismic Q observations in the lithosphere between 1 and 30 Hz: Geophysical Research Letters, v. 8, p. 1126–1128, https://doi.org/10.1029/GL008i011p01126.

Delph, J.R., Zandt, G., and Beck, S.L., 2015, A new approach to obtaining a 3D shear wave velocity model of the crust and upper mantle: An application to eastern Turkey: Tectonophysics, v. 665, p. 92–100, https://doi.org/10.1016/j.tecto.2015.09.031.

Delph, J.R., Abgarmi, B., Ward, K.M., Beck, S.L., Özacar, A.A., Zandt, G., Sandvol, E., Türkelli, N., and Kalafat, D., 2017, The effects of subduction termination on the continental lithosphere: Linking volcanism, deformation, surface uplift, and slab tearing in central Anatolia: Geosphere, v. 13, p. 1788–1805, https://doi.org/10.1130/GES01478.1.

Faul, U.H., Fitz Gerald, J.D., and Jackson, I., 2004, Shear wave attenuation and dispersion in melt-bearing olivine polycrystals: 2. Microstructural interpretation and seismological implications: Journal of Geophysical Research, v. 109, B06202, https://doi.org/10.1029/2003JB002407.

Fehler, M., Hoshiba, M., Sato, H., and Obara, K., 1992, Separation of scattering and intrinsic attenuation for the Kanto-Tokai region, Japan, using measurements of *S*-wave energy versus hypocentral distance: Geophysical Journal International, v. 108, p. 787–800, https://doi.org/10.1111/j.1365-246X.1992.tb03470.x.

Gök, R., Sandvol, E., Türkelli, N., Seber, D., and Barazangi, M., 2003, Sn attenuation in the Anatolian and Iranian Plateau and surrounding regions: Geophysical Research Letters, v. 30, 8042, https://doi.org/10.1029/2003GL018020.

Gök, R., Pasyanos, M.E., and Zor, E., 2007, Lithospheric structure of the continent-continent collision zone: Eastern Turkey: Geophysical Journal International, v. 169, p. 1079–1088, https://doi.org/10.1111/j.1365-246X.2006.03288.x.

Gök, R., Mellors, R.J., Sandvol, E., Pasyanos, M., Hauk, T., Takedatsu, R., Yetirmishli, G., Teoman, U., Türkelli, N., Godoladze, T., and Javakishvirli, Z., 2011, Lithospheric velocity structure of the Anatolian plateau–Caucasus–Caspian region: Journal of Geophysical Research, v. 116, B05303, https://doi.org/10.1029/2009JB000837.

Granot, R., 2016, Palaeozoic oceanic crust preserved beneath the eastern Mediterranean: Nature Geoscience, v. 9, p. 701–705, https://doi.org/10.1038/ngeo2784.

Hafkenscheid, E., Wortel, M.J.R., and Spakman, W., 2006, Subduction history of the Tethyan region derived from seismic tomography and tectonic reconstructions: Journal of Geophysical Research, v. 111, B08401, https://doi.org/10.1029/2005JB003791.

Halpaap, F., Rondenay, S., and Ottemöller, L., 2018, Seismicity, deformation, and metamorphism in the Western Hellenic Subduction Zone: New constraints from tomography: Journal of Geophysical Research: Solid Earth, v. 123, p. 3000–3026, https://doi.org/10.1002/2017JB015154.

Hatzfeld, D., and Molnar, P., 2010, Comparisons of the kinematics and deep structures of the Zagros and Himalaya and of the Iranian and Tibetan Plateaus and geodynamic implications: Reviews of Geophysics, v. 48, https://doi.org/10.1029/2009RG000304.

Hearn, T.M., and Ni, J., 1994, *Pn* velocities beneath continental collision zones: The Turkish-Iranian Plateau: Geophysical Journal International, v. 117, p. 273–283, https://doi.org/10.1111/j.1365-246X.1994.tb03931.x.

Innocenti, F., Mazzuoli, G., Pasquarè, F., Radicati Di Brozolo, F., and Villari, L., 1975, The Neogene calcalkaline volcanism of Central Anatolia: Geochronological data on Kayseri-Niğde area: Geological Magazine, v. 112, p. 349–360, https://doi.org/10.1017/S0016756800046744.

Isacks, B.L., and Stephens, C., 1975, Conversion of Sn to Lg at a continental margin: Bulletin of the Seismological Society of America, v. 65, p. 235–244, https://doi.org/10.1785/BSSA0650010235.

Jackson, I., Fitz Gerald, J.D., Faul, U.H., and Tan, B.H., 2002a, Grain-size-sensitive seismic wave attenuation in polycrystalline olivine: Journal of Geophysical Research, v. 107, 2360, https://doi.org/10.1029/2001JB001225.

Jackson, I., Faul, U.H., Fitz Gerald, J.D., and Tan, B.H., 2004, Shear wave attenuation and dispersion in melt-bearing olivine polycrystals: 1. Specimen fabrication and mechanical testing: Journal of Geophysical Research, v. 109, B06201, https://doi.org/10.1029/2003JB002406.

Jackson, J., Priestley, K., Allen, M., and Berberian, M., 2002b, Active tectonics of the South Caspian Basin: Geophysical Journal International, v. 148, p. 214–245, https://doi.org/10.1046/j.1365-246X.2002.01005.x.

Kadinsky-Cade, K., Barazangi, M., Oliver, J., and Isacks, B., 1981, Lateral variations of high-frequency seismic wave propagation at regional distances across the Turkish and Iranian Plateaus: Journal of Geophysical Research, v. 86, p. 9377–9396, https://doi.org/10.1029/JB086iB10p09377.

Kaviani, A., Paul, A., Bourova, E., Hatzfeld, D., Pedersen, H., and Mokhtari, M., 2007, A strong seismic velocity contrast in the shallow mantle across the Zagros collision zone (Iran): Geophysical Journal International, v. 171, p. 399–410, https://doi.org/10.1111/j.1365-246X.2007.03535.x.

Kaviani, A., Sandvol, E., Bao, X.Y., Rümpker, G., and Gök, R., 2015, The structure of the crust in the Turkish-Iranian Plateau and Zagros using Lg *Q* and velocity: Geophysical Journal International, v. 200, p. 1254–1268, https://doi.org/10.1093/gji/ggu468.

Kaviani, A., Paul, A., Moradi, A., Mai, P.M., Pilia, S., Boschi, L., Rümper, G., Lu, Y., Tang, Z., and Sandvol, E., 2020, Crustal and uppermost mantle shear wave velocity structure beneath the Middle East from surface wave tomography: Geophysical Journal International, v. 221, p. 1349–1365, https://doi.org/10.1093/gji/ggaa075.

Kaviani, A., Mahmoodabadi, M., Rümpker, G., Pilia, S., Tatar, M., Nilfouroushan, F., Yamini-Fard, F., Moradi, A., and Ali, M.Y., 2021, Mantle-flow diversion beneath the Iranian Plateau induced by Zagros' lithospheric keel: Scientific Reports, v. 11, 2848, https://doi.org/10.1038/s41598-021-81541-9.

Keskin, M., 2003, Magma generation by slab steepening and breakoff beneath a subduction accretion complex: An alternative model for collision-related volcanism in eastern Anatolia, Turkey: Geophysical Research Letters, v. 30, 8046, https://doi.org/10.1029/2003GL018019.

Knapp, C.C., Knapp, J.H., and Connor, J.A., 2004, Crustal-scale structure of the South Caspian Basin revealed by deep seismic reflection profiling: Marine and Petroleum Geology, v. 21, p. 1073–1081, https://doi.org/10.1016/j.marpetgeo.2003.04.002.

Knopoff, L., Aki, K., Archambeau, C.B., Ben-Menahem, A., and Hudson, J.A., 1964, Attenuation of dispersed waves: Journal of Geophysical Research, v. 69, p. 1655–1657, https://doi.org/10.1029/JZ069i008p01655.

Maggi, A., and Priestley, K., 2005, Surface waveform tomography of the Turkish-Iranian Plateau: Geophysical Journal International, v. 160, p. 1068–1080, https://doi.org/10.1111/j.1365-246X.2005.02505.x.

Mahmoodabadi, M., Yaminifard, F., Tatar, M., Kaviani, A., and Motaghi, K., 2019, Upper-mantle velocity structure beneath the Zagros collision zone, Central Iran and Alborz from nonlinear teleseismic tomography: Geophysical Journal International, v. 218, p. 414–428, https://doi.org/10.1093/gji/ggz160.

Martynov, G.V., Vernon, F.L., Mellors, R.J., and Pavlis, G.L., 1999, High-frequency attenuation in the crust and upper mantle of the northern Tien Shan: Bulletin of the Seismological Society of America, v. 89, p. 215–238, https://doi.org/10.1785/BSSA0890010215.

McKenzie, D., and Priestley, K., 2016, Speculations on the formation of cratons and cratonic basins: Earth and Planetary Science Letters, v. 435, p. 94–104, https://doi.org/10.1016/j.epsl.2015.12.010.

Molnar, P., and Oliver, J., 1969, Lateral variations of attenuation in the upper mantle and discontinuities in the lithosphere: Journal of Geophysical Research, v. 74, p. 2648–2682, https://doi.org/10.1029/JB074i010p02648.

Motaghi, K., Shabanian, E., and Kalvandi, F., 2017, Underplating along the northern portion of the Zagros suture zone, Iran: Geophysical Journal International, v. 210, p. 375–389, https://doi.org/10.1093/gji/ggx168.

Mouthereau, F., 2011, Timing of uplift in the Zagros belt/Iranian Plateau and accommodation of late Cenozoic Arabia-Eurasia convergence: Geological Magazine, v. 148, p. 726–738, https://doi.org/10.1017/S0016756811000306.

Mutlu, A.K., and Karabulut, H., 2011, Anisotropic Pn tomography of Turkey and adjacent regions: Geophysical Journal International, v. 187, p. 1743–1758, https://doi.org/10.1111/j.1365-246X.2011.05235.x.

Nakajima, J., and Hasegawa, A., 2003, Estimation of thermal structure in the mantle wedge of northeastern Japan from seismic attenuation data: Geophysical Research Letters, v. 30, 1760, https://doi.org/10.1029/2003GL017185.

Okay, A.I., and Tüysüz, O., 1999, Tethyan sutures of northern Turkey, *in* Durand, B., Jolivet, L., Horváth, F., and Séranne, M., eds., The Mediterranean Basins: Tertiary Extension within the Alpine Orogen: Geological Society of London Special Publication 156, p. 475–515, https://doi.org/10.1144/GSL.SP.1999.156.01.22.

Paige, C.C., and Saunders, M.A., 1982, LSQR: An algorithm for sparse linear equations and sparse least squares: ACM Transactions on Mathematical Software, v. 8, p. 43–71, https://doi.org/10.1145/355984.355989.

Pasyanos, M.E., Matzel, E.M., Walter, W.R., and Rodgers, A.J., 2009, Broad-band *Lg* attenuation modelling in the Middle East: Geophysical Journal International, v. 177, p. 1166–1176, https://doi.org/10.1111/j.1365-246X.2009.04128.x.

Paul, A., Kaviani, A., Hatzfeld, D., Vergne, J., and Mokhtari, M., 2006, Seismological evidence for crustal-scale thrusting in the Zagros mountain belt (Iran): Geophysical Journal International, v. 166, p. 227–237, https://doi.org/10.1111/j.1365-246X.2006.02920.x.

Paul, A., Hatzfeld, D., Kaviani, A., Tatar, M., and Péquegnat, C., 2010, Seismic imaging of the lithospheric structure of the Zagros mountain belt (Iran), *in* Leturmy, P., and Robin, C., eds., Tectonic and Stratigraphic Evolution of Zagros and Makran during the Mesozoic–Cenozoic: Geological Society of London Special Publication 330, p. 5–18, https://doi.org/10.1144/SP330.2.

Portner, D.E., Delph, J.R., Biryol, C.B., Beck, S.L., Zandt, G., Özacar, A.A., Sandvol, E., and Türkelli, N., 2018, Subduction termination through progressive slab deformation across Eastern Mediterranean subduction zones from updated P-wave tomography beneath Anatolia: Geosphere, v. 14, p. 907–925, https://doi.org/10.1130/GES01617.1.

Priestley, K., and McKenzie, D., 2013, The relationship between shear wave velocity, temperature, attenuation and viscosity in the shallow part of the mantle: Earth and Planetary Science Letters, v. 381, p. 78–91, https://doi.org/10.1016/j.epsl.2013.08.022.

Priestley, K., McKenzie, D., Barron, J., Tatar, M., and Debayle, E., 2012, The Zagros core: Deformation of the continental lithospheric mantle: Geochemistry Geophysics Geosystems, v. 13, Q11014, https://doi.org/10.1029/2012GC004435.

Reid, M.R., Schleiffarth, W.K., Cosca, M.A., Delph, J.R., Blichert-Toft, J., and Cooper, K.M., 2017, Shallow melting of MORB-like mantle under hot continental lithosphere, central Anatolia: Geochemistry Geophysics Geosystems, v. 18, p. 1866–1888, https://doi.org/10.1002/2016GC006772.

Reid, M.R., Delph, J.R., Cosca, M.A., Schleiffarth, W.K., and Gençalioğlu Kuşcu, G., 2019, Melt equilibration depths as sensors of lithospheric thickness during Eurasia-Arabia collision and the uplift of the Anatolian Plateau: Geology, v. 47, p. 943–947, https://doi.org/10.1130/G46420.1.

Rodgers, A.J., Ni, J.F., and Hearn, T.M., 1997, Propagation characteristics of short-period Sn and Lg in the Middle East: Bulletin of the Seismological Society of America, v. 87, no. 2, p. 396–413.

Salaün, G., Pedersen, H.A., Paul, A., Farra, V., Karabulut, H., Hatzfeld, D., Papazachos, C., Childs, D.M., Pequegnat, C., and the SIMBAAD team, 2012, High-resolution surface wave tomography beneath the Aegean-Anatolia region: Constraints on upper-mantle structure: Geophysical Journal International, v. 190, p. 406–420, https://doi.org/10.1111/j.1365-246X.2012.05483.x.

Sandvol, E., Al-Damegh, K., Calvert, A., Seber, D., Barazangi, M., Mohamad, R., Gök, R., Türkelli, N., and Gürbüz, C., 2001, Tomographic imaging of Lg and Sn propagation in the Middle East: Pure and Applied Geophysics, v. 158, p. 1121–1163, https://doi.org/10.1007/PL00001218.

Sato, H., Fehler, M.C., and Maeda, T., 2012, Seismic Wave Propagation and Scattering in the Heterogeneous Earth (second edition): Berlin, Heidelberg, Springer, 496 p., https://doi.org/10.1007/978-3-642-23029-5.

Schleiffarth, W.K., Darin, M.H., Reid, M.R., and Umhoefer, P.J., 2018, Dynamics of episodic Late Cretaceous–Cenozoic magmatism across Central to Eastern Anatolia: New insights from an extensive geochronology compilation: Geosphere, v. 14, p. 1990–2008, https://doi.org/10.1130/GES01647.1.

Segev, A., Sass, E., and Schattner, U., 2018, Age and structure of the Levant basin, Eastern Mediterranean: Earth-Science Reviews, v. 182, p. 233–250, https://doi.org/10.1016/j.earscirev.2018.05.011.

Şengör, A.M.C., Özeren, S., Genç, T., and Zor, E., 2003, East Anatolian high plateau as a mantle-supported, north-south shortened domal structure: Geophysical Research Letters, v. 30, 8045, https://doi.org/10.1029/2003GL017858.

Şengör, A.M.C., Tüysüz, O., İmren, C., Sakınç, M., Eyidoğan, H., Görür, N., Le Pichon, X., and Rangin, C., 2005, The North Anatolian Fault: A new look: Annual Review of Earth and Planetary Sciences, v. 33, p. 37–112, https://doi.org/10.1146/annurev.earth.32.101802.120415.

Shito, A., Karato, S., and Park, J., 2004, Frequency dependence of *Q* in Earth's upper mantle inferred from continuous spectra of body waves, Geophysical Research Letters, v. 31, L12603, https://doi.org10.1029/2004GL019582.

Simmons, N.A., Myers, S.C., and Johannesson, G., 2011, Global-scale *P* wave tomography optimized for prediction of teleseismic and regional travel times for Middle East events: 2. Tomographic inversion: Journal of Geophysical Research, v. 116, B04305, https://doi.org/10.1029/2010JB007969.

Stephens, C., and Isacks, B.L., 1977, Toward an understanding of Sn: Normal modes of Love waves in an oceanic structure: Bulletin of the Seismological Society of America, v. 67, p. 69–78.

Stöcklin, J., 1968, Structural history and tectonics of Iran: A review: American Association of Petroleum Geologists Bulletin, v. 52, p. 1229–1258, https://doi.org/10.1306/5D25C4A5-16C1-11D7-8645000102C1865D.

Tiwari, A.K., Singh, C., Sandvol, E., Mukhopadhyay, S., Singh, A., and Gupta, A.K., 2022, Sn attenuation tomography of southeastern Tibet: New constraints on lithospheric mantle deformation: Geophysical Journal International, v. 228, p. 1038–1053, https://doi.org/10.1093/gji/ggab380.

Vernant, P., Nilforoushan, F., Hatzfeld, D., Abbassi, M.R., Vigny, C., Masson, F., Nankali, H., Martinod, J., Ashtiani, A., Bayer, R., Tavakoli, F., and Chéry, J., 2004, Present-day crustal deformation and plate kinematics in the Middle East constrained by GPS measurements in Iran and northern Oman: Geophysical Journal International, v. 157, p. 381–398, https://doi.org/10.1111/j.1365-246X.2004.02222.x.

Xia, S.H., Sun, J.L., and Huang, H.B., 2015, Degree of serpentinization in the forearc mantle wedge of Kyushu subduction zone: Quantitative evaluations from seismic velocity: Marine Geophysical Researches, v. 36, p. 101–112, https://doi.org/10.1007/s11001-014-9239-3.

Xie, J., and Mitchell, B.J., 1990, A back-projection method for imaging large-scale lateral variations of *Lg* coda *Q* with application to continental Africa: Geophysical Journal International, v. 100, p. 161–181, https://doi.org/10.1111/j.1365-246X.1990.tb02477.x.

Yang, X.N., Lay, T., Xie, X.B., and Thorne, M.S., 2007, Geometric spreading of Pn and Sn in a spherical Earth model: Bulletin of the Seismological Society of America, v. 97, p. 2053–2065, https://doi.org/10.1785/0120070031.

Zor, E., Sandvol, E., Xie, J.K., Türkelli, N., Mitchell, B., Gasanov, A.H., and Yetirmishli, G., 2007, Crustal attenuation within the Turkish Plateau and surrounding regions: Bulletin of the Seismological Society of America, v. 97, p. 151–161, https://doi.org/10.1785/0120050227.